

Frequency Beamforming-Enhanced DBIM for Limited-Aperture Quantitative Imaging

Scott J. Ziegler¹ and Matthew J. Burfeindt, *Senior Member, IEEE*

Abstract—The distorted Born iterative method (DBIM) is a technique for reconstructing a dielectric profile from scattered electric fields. The potential for effective imaging with DBIM has been demonstrated for a variety of applications. However, it is more challenging to reliably produce high-fidelity imagery when the aperture formed by the sensors does not fully surround the region of interest and when data is collected over a narrow bandwidth. To address this challenge, we propose a beamforming enhancement to DBIM for limited-aperture scenarios. The beamforming enhancement pre-focuses the data prior to performing the DBIM optimization in order to achieve a better-conditioned inversion. The enhancement is an advance on previous beamforming work for DBIM in that it focuses simultaneously across not only space but also frequency, which allows for better leveraging of range information in the limited-aperture signal. Results for simulated and experimental data demonstrate that the frequency beamforming enhancement to DBIM results in less sensitivity to the choice of the regularization parameter and produces better reconstructions when spatial and frequency information is limited.

Index Terms—Electromagnetic propagation, inverse problems, radar theory, signal processing.

I. INTRODUCTION

ELECTROMAGNETIC quantitative inverse scattering (QIS) is the process of recovering both a target's shape and dielectric profile from scattered electric fields. We include the term quantitative to contrast with qualitative inverse scattering methods, which seek to reconstruct only the support of the target. The additional information concerning the dielectric profile in QIS allows for potential applications in numerous fields of study, including non-destructive evaluation [1], ground-penetrating radar [2], and medical imaging [3]. QIS problems are difficult due to the high degree of ill-posedness inherent in the problem, which necessitates regularization. The inversion is often very sensitive to the choice of the regularization parameter, and effectively selecting the regularization parameter may be more difficult as the degree of ill-posedness increases due to practical limits on data diversity. Methods for quantitative inversion must overcome this difficulty in order to be useful.

Received 1 April 2024; revised 4 December 2024; accepted 26 December 2024. Date of publication 13 January 2025; date of current version 5 February 2025. This work was supported by the Office of Naval Research via the Naval Research Laboratory (NRL) 6.2 Base Program. (*Corresponding author: Scott J. Ziegler.*)

The authors are with the United States Naval Research Laboratory, Washington, DC 20375 USA (e-mail: scott.ziegler@nrl.navy.mil; matthew.burfeindt@nrl.navy.mil).

Digital Object Identifier 10.1109/TAP.2025.3526904

There has been extensive work in developing efficient and robust techniques for QIS in a full-aperture setting. Ray-based tomographic methods [4], [5] use high-frequency approximations and backprojection techniques to obtain an image. These algorithms are typically fast and easy to implement, but neglect multiple scattering within an imaging domain resulting in poor reconstructions for complex targets and low-frequency data. Full waveform inversion methods [6], [7], [8] minimize a fully nonlinear loss function and solve the wave equation multiple times at each iteration, which results in high-fidelity reconstructions at a large computational expense. The modified gradient method [9] and its later offspring the contrast source inversion method [10] seek to minimize a nonlinear functional and avoid the need for forward solvers. The Born iterative method [11] is the forerunner of the distorted Born iterative method (DBIM) [12], which linearizes an integral equation using the Born approximation at each step of an iterative algorithm. The primary difference between the Born iterative method and DBIM is that in DBIM the Green's function is updated at each iteration, resulting in faster convergence and sharper reconstructions. Thus, DBIM possesses a nice mixture of high fidelity capabilities with moderate computational complexity.

In an ideal imaging scenario, the target is fully surrounded by antennas and data is collected across multiple widely-spaced frequencies, resulting in a dataset with significant spatial and frequency diversity. This diversity mitigates the ill-posed nature of the inverse problem, leading to higher-fidelity reconstructions that are more robust to small parameter changes. However, there are many practical scenarios in which it may not be possible to surround the target by sensors. For example, we may not physically have access to all sides of the target due to a barrier or the object being buried underground. There could also be prohibitive costs in spreading sensors over a large area, or if few overall sensors are used, it may not be desirable to spread them out due to the possibility of introducing azimuth ambiguities into the data. The restriction of viewing angles that accompanies limited-aperture imaging increases the ill-posedness of the problem by reducing spatial information in the scattering data. For cost reasons, many real-world systems may transmit and receive data over a narrow bandwidth as opposed to using a few widely spaced frequencies. This is true, for example, of traditional radar systems. The use of a limited bandwidth with closely spaced frequencies causes frequency information redundancy in the data, serving to once again heighten the

ill-posedness of the problem. This reduction of spatial and frequency information manifests itself through heightened sensitivity to noise, model error, and parameter selection.

Recent research shows an interest in overcoming the difficulties inherent in limited-aperture imaging for both qualitative and QIS problems. Liu and Sun [13] use a data recovery algorithm to approximate full-aperture data before using the direct sampling method [14], [15] to obtain a qualitative reconstruction. Kang et al. [16] also explore the direct sampling method for limited apertures with transverse magnetic incident waves by introducing a novel indicator function specifically designed for limited-aperture data. This was extended upon in [17] with the design of an indicator function for the direct sampling method with limited-aperture data for transverse electric incident waves. Park [18] investigates the Multiple Signal Classification (MUSIC) algorithm [19], [20] for imaging small circular inhomogeneities in a limited-aperture setting. Benedetti et al. [21] also attempt to qualitatively detect and reconstruct anomalies in dielectric materials by first obtaining a region-of-interest reconstruction and then refining the reconstruction using a level-set algorithm. Burfeindt and Alqadah [22] introduce a propagation-based phase encoding to the linear sampling method [23] in order to improve imaging performance in a limited-aperture setting. Audibert and Haddar [24] analyze the generalized linear sampling method [25] for limited-aperture data at a single frequency by introducing a novel penalty term to the problem formulation. The work presented in [26] is unique in its incorporation of inverse tomographic techniques to ground penetrating radar (GPR). The authors assume far-field measurements and apply the Born approximation in order to linearize and reconstruct a contrast function, but are only interested in the location and size of buried objects as opposed to their dielectric properties.

The analysis of quantitative inversion techniques using a limited aperture has primarily been applied to GPR and medical imaging. In [27], an overview of both qualitative and quantitative techniques for GPR is given with an emphasis on overcoming the nonlinearity and ill-posedness that is caused in part by a limited-aperture measurement scenario. The work in [28] considers both the linear sampling method and the Born approximation method [29] for GPR data by introducing a multifrequency processing step and a regularization technique based on the theory of compressive sensing. A hybrid approach for subsurface imaging is adopted in [30] by first obtaining a qualitative reconstruction using LSM, sharpening the reconstruction using a convolutional neural network, and then performing a quantitative reconstruction using the Born iterative method. Another hybrid approach is presented in [31], where the authors compensate for a lack of tomographic data in the contrast source inversion method by incorporating information from the traditional radar technique called range points migration. Bevacqua et al. [33] analyze quantitative medical imaging using the Born approximation method, but build an indicator function out of the resulting reconstruction which is normalized by the energy in the Green's function in order to account for the limited aperture. These previous quantitative inversion methods in limited-aperture settings typically make use of prior information either by utilizing

a multistep approach or through the inclusion of a penalty term.

In this article, we propose a new strategy for mitigating the challenges of limited apertures, limited bandwidths, and close frequency spacings. Our strategy involves pre-focusing the electric field via a beamforming operation prior to performing the DBIM optimization. We hypothesize that the beamforming operation lowers the complexity of the solution space by emphasizing regions in the imaging domain corresponding to strong signal return. This stabilizes the solution for scenarios with limited data diversity.

Our implementation is an advancement to a previously introduced beamforming enhancement to DBIM that was presented for a medical imaging application [34]. In this prior work, the antennas completely surrounded the imaging domain and collected data across a wide span of frequencies (1.5 GHz). The beamforming operation was applied at each collected frequency individually. Our enhancement for limited-apertures and a band of closely spaced frequencies is to simultaneously perform the beamforming operation across both space and frequency. Focusing signals across a band of frequencies is a conventional radar method for achieving resolution in the range direction, i.e., the direction orthogonal to the array, and thus is of interest for improving the performance of limited-aperture imaging. In addition, this strategy leverages the information redundancy of closely spaced frequencies, as focusing across small frequency increments mitigates aliasing in the range direction in traditional radar focusing. This approach differs from the use of radar techniques as seen in [31] because rather than alternate between a range-determination procedure and a quantitative method, we inject the range focusing directly into the DBIM algorithm, thus avoiding the need for multiple algorithms on a single scene.

In [35], we outlined the mathematics behind the frequency beamforming enhancement and presented results from a single scatterer at one aperture orientation. This work extends on those preliminary results by giving a more detailed description of the beamforming scheme as well as presenting results from additional numerical targets at a variety of aperture and SNR values and includes experimental results using the University of Manitoba microwave imaging dataset [38]. Our work is distinct from previous quantitative limited-aperture work [27], [28], [29], [30] in that it does not utilize prior information nor introduce a new regularization term, but alters the formation of the problem itself. Reconstructions using both simulated and experimental data reveal that, for limited-aperture scenarios, our approach is able to decrease the sensitivity of the DBIM algorithm to regularization parameter, aperture size, and noise. We proceed by describing the proposed method in Section II, displaying results from simulated data in Section III and experimental data in Section IV, and discussing relevant conclusions and future work in Section V.

II. BEAMFORMING-DBIM

A. Distorted Born Iterative Method

DBIM is an iterative reconstruction technique that uses successive linearizations of the total electric field and updates

of the dyadic Green's function in order to build an approximation of the dielectric properties of a region of interest Ω . For the duration of this article, $\Omega \subset \mathbb{R}^2$, but the technique can be extended to \mathbb{R}^3 in a natural way. The propagation of a monochromatic wave in a medium is governed by the Helmholtz equation. Beginning with the integral solution to the Helmholtz equation, we have

$$E_{sc}(\mathbf{r}_T, \mathbf{r}_O; \omega) = \omega^2 \epsilon_0 \mu_0 \int_{\Omega} G_b(\mathbf{r}_O, \mathbf{r}'; \omega) E_{tot}(\mathbf{r}_T, \mathbf{r}'; \omega) \delta\rho(\mathbf{r}') d\mathbf{r}' \quad (1)$$

where E_{sc} and E_{tot} are the scattered and total electric fields, \mathbf{r}_T and \mathbf{r}_O are the locations of the transmitting and receiving antennas, ω is the angular frequency, ϵ_0 and μ_0 are the background permittivity and permeability, G_b is the dyadic Green's function, and $\delta\rho(\mathbf{r}') = \delta\epsilon_r(\mathbf{r}') - i(\delta\sigma_b(\mathbf{r}')/\omega\epsilon_0)$ is the dielectric contrast, with $\delta\epsilon_r$ being the contrast in relative permittivity with the background and $\delta\sigma_b$ the contrast in conductivity with the background.

In DBIM, the first step is to linearize (1) by taking the Born approximation, replacing the total electric field under the integral by the incident electric field E_{in} . This yields

$$E_{sc}(\mathbf{r}_T, \mathbf{r}_O; \omega) = \omega^2 \epsilon_0 \mu_0 \int_{\Omega} G_b(\mathbf{r}_O, \mathbf{r}'; \omega) E_{in}(\mathbf{r}_T, \mathbf{r}'; \omega) \delta\rho(\mathbf{r}') d\mathbf{r}'. \quad (2)$$

Note that while there are generally conditions for applying the Born approximation (see [32], for example), DBIM avoids these conditions by making no assumptions about the medium and taking nonlinearities into account through an iterative process. Equation (2) is discretized to form the linear system $\mathbf{A}(\omega)\mathbf{x} = \mathbf{b}(\omega)$, where $\mathbf{A}(\omega)$ represents the integral operator at frequency ω , \mathbf{x} contains the values of $\delta\rho$ on each pixel, and \mathbf{b} holds the scattered electric field data at frequency ω . Multiple frequencies $\omega_1, \dots, \omega_F$ can be incorporated by either stacking matrices $\mathbf{A}(\omega_f)$ and vectors $\mathbf{b}(\omega_f)$ to form the larger system denoted as $\mathbf{A}_S\mathbf{x} = \mathbf{b}_S$, or by using the reconstruction at a lower frequency as a starting estimate for the algorithm at higher frequencies. The latter approach can be beneficial for difficult imaging scenarios, as the inverse problem is less ill-posed at lower frequencies. However, this technique often requires more iterations for the same number of frequencies.

In this work, we implement a hybrid version of these approaches by partitioning the set of frequencies $\omega_1, \dots, \omega_F$ into batches S_1, S_2, \dots, S_K , where S_1 contains the first N_1 frequencies, S_2 contains the next N_2 frequencies, and so on. We then form the linear system $\mathbf{A}_{S_1}\mathbf{x} = \mathbf{b}_{S_1}$ by stacking the matrices $\mathbf{A}(\omega_f)$ and vectors $\mathbf{b}(\omega_f)$ formed from the first N_1 frequencies, and use the solution with this batch of frequencies as the starting point for the next batch. In this work, we choose a narrower band for S_1 compared to S_k , $k > 1$ in order to provide a compromise between the stability afforded by limiting the first band to lower frequencies with the enhanced range information afforded by wider bandwidths in the upper bands. After adding a Tikhonov regularization term, we write the solution to the linear system using frequency

batch S_k as

$$\mathbf{x} = \operatorname{argmin}_{\tilde{\mathbf{x}}} \{ \|\mathbf{A}_{S_k}\tilde{\mathbf{x}} - \mathbf{b}_{S_k}\|_2^2 + \alpha \|\tilde{\mathbf{x}}\|_2^2 \} \quad (3)$$

where α is a regularization parameter.

For F given matrices of bistatic scattering data $\{\mathcal{D}(\omega_f) \mid f = 1, \dots, F\}$, the DBIM algorithm begins by choosing a partitioning of the frequencies and selecting a starting value of the dielectric properties ρ_0 . The incident field and Green's function are then computed to form the linear system $\mathbf{A}_{S_1}\mathbf{x} = \mathbf{b}_{S_1}$, the minimization problem in (3) is solved, the dielectric properties are updated through $\rho_{i+1} = \rho_i + \delta\rho_i$, and these steps recur until a termination condition is reached. This process is then repeated for each of the $K - 1$ remaining frequency batches, using the resulting dielectric properties from the previous batch as the starting point for the next batch.

B. DBIM With Spatial Beamforming Enhancement

In order to describe the spatial beamforming enhancement to DBIM [34], we first introduce the following notation. Let

$$\begin{aligned} \mathbf{e}_{in}(\mathbf{r}'; \omega) &= [E_{in}(\mathbf{r}_1, \mathbf{r}'; \omega) \dots E_{in}(\mathbf{r}_J, \mathbf{r}'; \omega)]^T \\ \mathbf{g}_b(\mathbf{r}'; \omega) &= [G_b(\mathbf{r}_1, \mathbf{r}'; \omega) \dots G_b(\mathbf{r}_J, \mathbf{r}'; \omega)]^T \end{aligned}$$

where $\{\mathbf{r}_j \mid j = 1, \dots, J\}$ are the locations of the J antennas used to transmit and receive data. Now, let $\mathbf{w}_{r_d} := \mathbf{g}_b(\mathbf{r}_d)/\|\mathbf{g}_b(\mathbf{r}_d)\|$ be a beamforming weight vector designed to focus the transmitted and received signals at location $\mathbf{r}_d \in \Omega$. We write the linear system at frequency ω and focused at location \mathbf{r}_d as

$$\begin{aligned} \mathbf{w}_{r_d}^H \mathcal{D}(\omega) \mathbf{w}_{r_d}^* &= \omega^2 \epsilon_0 \mu_0 \int_{\Omega} \mathbf{w}_{r_d}^H \mathbf{e}_{in}(\mathbf{r}'; \omega) \mathbf{g}_b^T(\mathbf{r}'; \omega) \mathbf{w}_{r_d}^* \delta\rho(\mathbf{r}') d\mathbf{r}' \end{aligned} \quad (4)$$

where the superscript H denotes the Hermitian transpose and $*$ denotes the complex conjugate. Equation (4) is replicated for a desired number of different focus locations and then discretized to give the linear system $\mathbf{A}_B(\omega)\mathbf{x} = \mathbf{b}_B(\omega)$. The construction of this linear system, including the treatment of the diagonal elements for which the Green's function becomes singular, is handled in [34]. After forming the matrices $\mathbf{A}_B(\omega)$ and focused data vectors $\mathbf{b}_B(\omega)$, the spatial beamforming-enhanced DBIM (SBE-DBIM) algorithm proceeds as in the standard DBIM algorithm with the beamformed linear system replacing the linear system $\mathbf{A}(\omega)\mathbf{x} = \mathbf{b}(\omega)$.

C. DBIM With Frequency Beamforming Enhancement

The conventional way to use multiple frequencies in SBE-DBIM is to stack the matrices $\mathbf{A}_B(\omega_1), \dots, \mathbf{A}_B(\omega_{N_1})$ and right-hand side vectors $\mathbf{b}_B(\omega_1), \dots, \mathbf{b}_B(\omega_{N_1})$ and solve the resulting linear system. This notation assumes that we are using the first batch of frequencies $(\omega_1, \dots, \omega_{N_1})$, but the formation is the same for the other frequency batches.

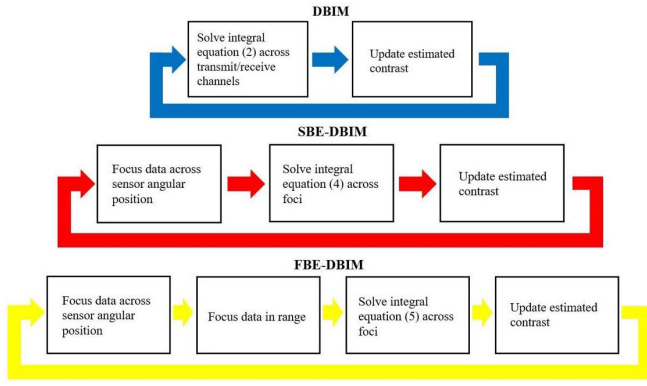


Fig. 1. Comparison of the primary steps taken in DBIM, SBE-DBIM, and FBE-DBIM.

We propose to instead add a focusing step across frequency, giving the linear system

$$\begin{aligned} & \int_{\omega_1}^{\omega_{N_1}} \mathbf{w}_{r_d}^H \mathcal{D}(\omega') \mathbf{w}_{r_d}^* d\omega' \\ &= \int_{\omega_1}^{\omega_{N_1}} (\omega')^2 \epsilon_0 \mu_0 \int_{\Omega} \mathbf{w}_{r_d}^H \mathbf{e}_{in}(\mathbf{r}'; \omega') \mathbf{g}_b^T(\mathbf{r}'; \omega') \mathbf{w}_{r_d}^* \delta \rho(\mathbf{r}') d\mathbf{r}' d\omega'. \end{aligned} \quad (5)$$

In discretized form, this simply gives

$$\left[\sum_{f=1}^{N_1} \mathbf{A}_B(\omega_f) \right] \mathbf{x} = \left[\sum_{f=1}^{N_1} \mathbf{b}_B(\omega_f) \right]. \quad (6)$$

This linear system replaces $\mathbf{A}_{S_1}(\omega) \mathbf{x} = \mathbf{b}_{S_1}(\omega)$ in the traditional multifrequency DBIM algorithm, and we refer to the algorithm with this focused linear system as frequency beamforming-enhanced DBIM (FBE-DBIM). Fig. 1 displays flowcharts outlining the main steps for standard DBIM, SBE-DBIM, and FBE-DBIM. We note that the linear system in (6) is guaranteed to not be larger than the linear system produced using only the spatial beamforming enhancement, providing potential benefits with regards to computational efficiency.

The coherent sum over frequencies in (6) after the use of the spatial beamforming enhancement is equivalent to range matched-filtering after focusing in azimuth for limited-aperture scenarios. This can be seen by considering a generic radar focusing operation in which we focus a received radar signal $S(\mathbf{r}_T, \mathbf{r}_O, \omega)$ at a location \mathbf{r} , where $\mathbf{r}_T, \mathbf{r}_O$ are again vectors of transmit and receive locations. The focusing operation over transmit locations, receive locations, and frequency is given by

$$I(\mathbf{r}) = \int \int \int S(\mathbf{r}_T, \mathbf{r}_O, \omega) e^{-i \frac{\omega}{c} ((\mathbf{r}-\mathbf{r}_T) + (\mathbf{r}-\mathbf{r}_O))} d\mathbf{r}_T d\mathbf{r}_O d\omega.$$

Performing the integration over \mathbf{r}_T and \mathbf{r}_O gives $I(\mathbf{r}) = \int S_C(\mathbf{r}, \omega) d\omega$, where S_C is the data focused across sensor position. Thus, this equation shows that the final focusing step across frequency can be performed by simply summing the signal that has already been focused across sensor position. We emphasize that both the spatial and frequency beamforming schemes we present have no plane wave assumptions, meaning these techniques are in principle valid in both the near and far-field.

In order to test the efficacy of the frequency beamforming enhancement in tandem with the spatial beamforming enhancement, we will also test a version of DBIM in which the linear system for the first frequency batch is formed using

$$\left[\sum_{f=1}^{N_1} \mathbf{A}(\omega_f) \right] \mathbf{x} = \left[\sum_{f=1}^{N_1} \mathbf{b}(\omega_f) \right]. \quad (7)$$

That is, the linear system is formed by summing over frequency without first focusing across sensor locations. For convenience, we refer to this method as frequency-summed DBIM (FS-DBIM).

III. NUMERICAL RESULTS

A. Data Simulation for Numerical Phantoms

In order to test the proposed frequency beamforming enhancement to DBIM, data was simulated using a 2-D transverse-magnetic finite-difference time-domain simulation with antennas distributed in 1° increments across a 180° aperture. The antennas were arranged over a radius of 6 m with the spatial discretization in both the x - and y -directions being 0.033 m. Data was simulated for six different target shape profiles: a lossless kite-shaped profile with a maximum diameter of 2.1 m and relative permittivity $\epsilon_r = 2$, a lossless single circle of radius 50 cm and relative permittivity $\epsilon_r = 2$, a lossy L-shaped profile with side lengths of 1.6 m, relative permittivity $\epsilon_r = 2$, and conductivity $\sigma = 10$ mS/m, a lossless L-shaped profile with side lengths of 1.6 m and relative permittivity $\epsilon_r = 2$, the same lossless L-shaped profile with a relative permittivity of $\epsilon_r = 5$, and a lossless double circle profile with each circle having the same radius of 50 cm but different relative permittivities of $\epsilon_r = 2$ and 3. For this work, we only considered the case in which the background has zero conductivity, but the technique could be extended to other situations in a natural way. Signal phasors were acquired from 100 to 405 MHz, with 5-MHz frequency spacing. Gaussian noise was added to the array of bistatic scattering data in order to simulate data with approximate SNR values of 42, 28, 14, and 0 dB.

B. Inversion Results

Reconstructions were run using the standard multifrequency DBIM algorithm, the SBE-DBIM algorithm, and the FBE-DBIM algorithm for each of the five shape profiles using datasets consisting of 30 bistatic channels across aperture sizes of 180° , 150° , 120° , and 90° . The orientation of these apertures against the single circle scatterer is shown in Fig. 2. In addition, reconstructions were also computed using the FS-DBIM algorithm for the kite-shaped scatterer, in order to determine the effect of summing over frequency without the spatial beamforming enhancement. The spatial discretization for the inverse problem was set to the coarser value of 0.1 m in order to avoid an inverse crime. After the selection of this coarser grid, a calibration step similar to the one performed in [36] was performed in order to better match the simulated data to the inversion grid.

For five of the six targets, the frequencies were partitioned into the three batches $S_1 = 100 - 145$ MHz,

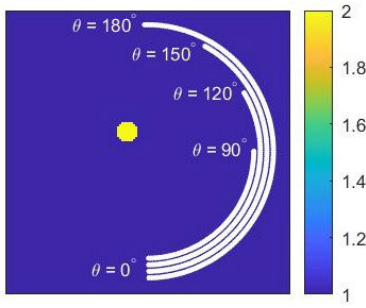


Fig. 2. Circle-shaped target with relative permittivity $\epsilon_r = 2$ and location of the different apertures used to collect data.

$S_2 = 150 - 255$ MHz, and $S_3 = 260 - 405$ MHz. The high-contrast L-shaped target used batch sizes of $S_1 = 100 - 175$ MHz, $S_2 = 180 - 275$ MHz, and $S_3 = 280 - 405$ MHz, as it was found that using a larger initial batch size improved results in this case. We hypothesized that using larger bandwidths for the higher frequency components would allow the FBE-DBIM algorithm to more easily garner range information in the limited-aperture setting. In order to test the robustness of the algorithms against the choice of regularization parameter, eight different values of α evenly spaced on a logarithmic scale from 10^{-6} to 10 were used for all of the noisy datasets. For both SBE-DBIM and FBE-DBIM, 169 beamforming foci were distributed in the domain with spacing 0.5 m in each direction. Fig. 3 displays the location of these foci overlaid on the profile of the L-shaped scatterer. This choice of foci was meant to guarantee that multiple focus locations occurred within or near each target to ensure that the signal was being focused in the correct locations, while keeping the number of focus locations reasonably small in order to reduce the size of the system matrices.

The initial values of the dielectric properties were set to match the homogeneous background ($\epsilon_r = 1$, $\sigma = 0$ mS/m). The minimization problem at each iteration was computed by forming the normal equations for each algorithm and solving the resulting linear system with MATLAB's built-in *linsolve* function. The termination condition was set to be either 20 iterations or until the relative residual error (RRE) increased for consecutive iterations. For the high-contrast target, the termination condition was increased to 200 iterations to accommodate the higher relative permittivity. The RRE for frequency batch k at iteration i is given by

$$RRE_i^k = \frac{\sum_{j=N_{k-1}+1}^{N_k} \|\mathbf{b}_{\text{comp},i}(\omega_f) - \mathbf{b}(\omega_f)\|}{\sum_{j=N_{k-1}+1}^{N_k} \|\mathbf{b}(\omega_f)\|} \quad (8)$$

where $\mathbf{b}_{\text{comp},i}$ are the computed scattered fields at the antenna locations using the dielectric properties ρ_i .

Reconstructions were run on an Intel¹ Xeon¹ CPU E5-2695 v2 with 24 total cores. The average number of iterations and time per iteration for each of the three methods across all combinations of target type, aperture size, SNR, and value of α is listed in Table I.

Due to the RRE termination condition and the tendency of FBE-DBIM to stabilize the reconstruction process,

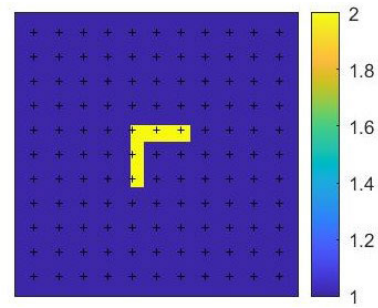


Fig. 3. Location of the 169 beamforming points in the imaging domain overlaid on the L-shaped scatterer with a relative permittivity $\epsilon_r = 2$.

TABLE I

AVERAGE NUMBER OF ITERATIONS AND TIME PER ITERATION FOR EACH OF THE THREE TESTED METHODS ACROSS ALL COMBINATIONS OF TARGETS, APERTURE SIZE, SNR, AND α VALUE

	Number of iterations	Time per iteration (seconds)
DBIM	19.11	664.03
SBE-DBIM	14.30	811.44
FBE-DBIM	31.19	483.86

FBE-DBIM averaged more iterations than either the standard DBIM or the SBE-DBIM algorithms. However, FBE-DBIM averaged less time per iteration compared with both standard DBIM and SBE-DBIM. This improvement in per-iteration computational performance is in part due to the batched frequency approach, as well as the termination condition that stops the reconstruction if the RRE increases for consecutive iterations. The initial iteration for each frequency batch requires the recomputation of frequency-dependent parameters, incurring an additional cost as compared to subsequent iterations using the same frequency batch. Since DBIM and SBE-DBIM were more sensitive to low values of the regularization parameter, those algorithms would often run for very few iterations at each frequency batch. This meant those algorithms spent a comparatively larger amount of time on the costly early iterations as compared to FBE-DBIM, yielding less efficient per-iteration computation times.

Another possible reason for the smaller per-iteration time in FBE-DBIM is the smaller size of the linear system [as displayed in (6)] as compared to the linear systems for DBIM and SBE-DBIM. In SBE-DBIM, the size of the matrices $\mathbf{A}_B(\omega)$ and right-hand side vectors $\mathbf{b}_B(\omega)$ are dependent on the size of the grid and number of beamforming foci established in the domain. For our examples, these matrices and right-hand side vectors were roughly five times smaller than the equivalent DBIM matrices $\mathbf{A}(\omega)$ and right-hand side vectors $\mathbf{b}(\omega)$. FBE-DBIM then sums the matrices $\mathbf{A}_B(\omega)$ and right-hand side vectors $\mathbf{b}_B(\omega)$ over frequency rather than stacking them, resulting in a linear system that is N_k times smaller than the equivalent SBE-DBIM system, where N_k is the number of frequencies used in the k th batch. Since solving the linear system is one of the most expensive steps at each iteration of each algorithm, the smaller system afforded by FBE-DBIM appears to contribute to improved per-iteration computational performance.

The top of Figs. 4–7 displays a subset of the reconstructions of relative permittivities for traditional DBIM, SBE-DBIM,

¹Registered trademark.

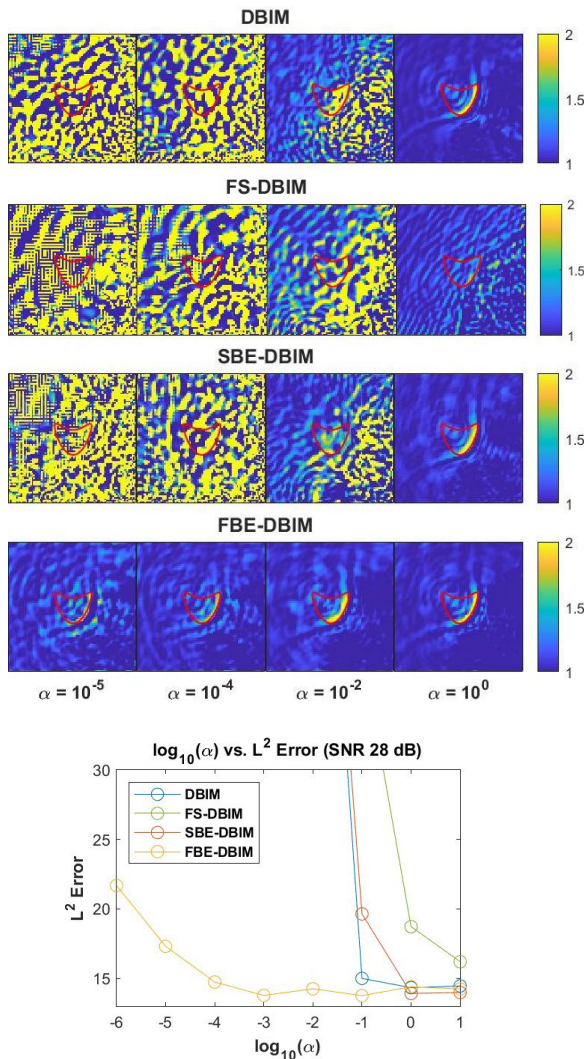


Fig. 4. Top: Reconstructed relative permittivity of kite-shaped target for four values of α with an SNR of 28 dB and an aperture size of 120°. Bottom: Plot of the L^2 error in the reconstructed relative permittivity against α .

and FBE-DBIM (and for the kite, FS-DBIM) at various aperture sizes for four different values of α . The top of Fig. 8 shows the reconstructed conductivity for the lossy L-shaped target. All displayed reconstructions in these figures used data with an SNR of 28 dB, and the outline of the true profile overlays each reconstruction. The plots in Figs. 5–8 show the values of the L^2 error of the difference between the reconstructed relative permittivity (or conductivity in Fig. 8) and true relative permittivity (conductivity) against the regularization parameter.

The first result that stands out when viewing these reconstructions is that the FBE-DBIM algorithm is much less sensitive to the choice of the regularization parameter compared with DBIM and SBE-DBIM. This is reflected both qualitatively in the reconstructed dielectric properties and quantitatively in the plots of the L^2 error against α . This phenomenon is seen especially clearly in the reconstruction for $\alpha = 10^{-6}$ in Fig. 5. The FBE-DBIM algorithm produces an image in which the target profile is still identifiable, compared with the nonsense produced by DBIM and SBE-DBIM. All three algorithms were not able to completely reconstruct the

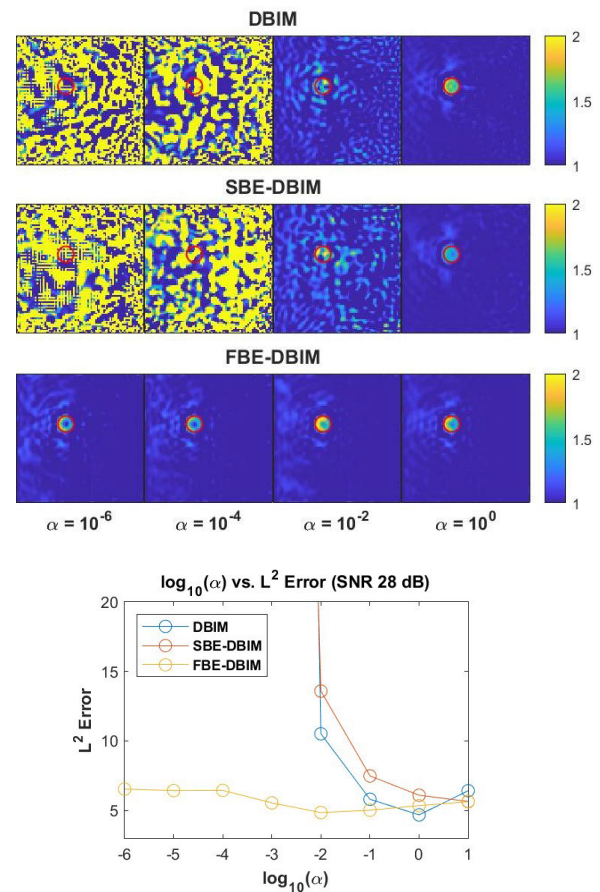


Fig. 5. Top: Reconstructed relative permittivity of single circle target for four values of α with an SNR of 28 dB and an aperture size of 180°. Bottom: Plot of the L^2 error in the reconstructed relative permittivity against α .

kite in Fig. 4, because less of the test volume is illuminated by the limited-aperture array due to its electrical thickness. However, the side of the kite closest to the antennas is visible in every FBE-DBIM reconstruction shown, whereas it is only visible in one of the reconstructions for both DBIM and SBE-DBIM. We also note that the FS-DBIM algorithm was unable to successfully reconstruct the target profile for any value of α , suggesting that summing over frequency without first performing the spatial beamforming enhancement is ineffective. For conciseness, later figures thus do not display results for FS-DBIM.

Fig. 6 reveals that the FBE-DBIM technique maintains its robustness against the choice of α in the high-contrast case and also gives the best overall reconstruction with respect to the L^2 error. The results are also interesting qualitatively, as the DBIM and SBE-DBIM reconstructions were only able to successfully reconstruct the corner scatterers of the L-shaped target, whereas FBE-DBIM better displays more of the overall shape of the target. This is displayed at the bottom of Fig. 6, which shows a zoomed-in and rescaled version of the reconstructions for all three algorithms at $\alpha = 10$. The FBE-DBIM algorithm captures the shape of the target with much higher fidelity and has less spurious artifacts surrounding the target as well. We note that in this example all three algorithms were unable to match the fidelity of the reconstructions for lower-contrast cases. This is a common issue for DBIM,

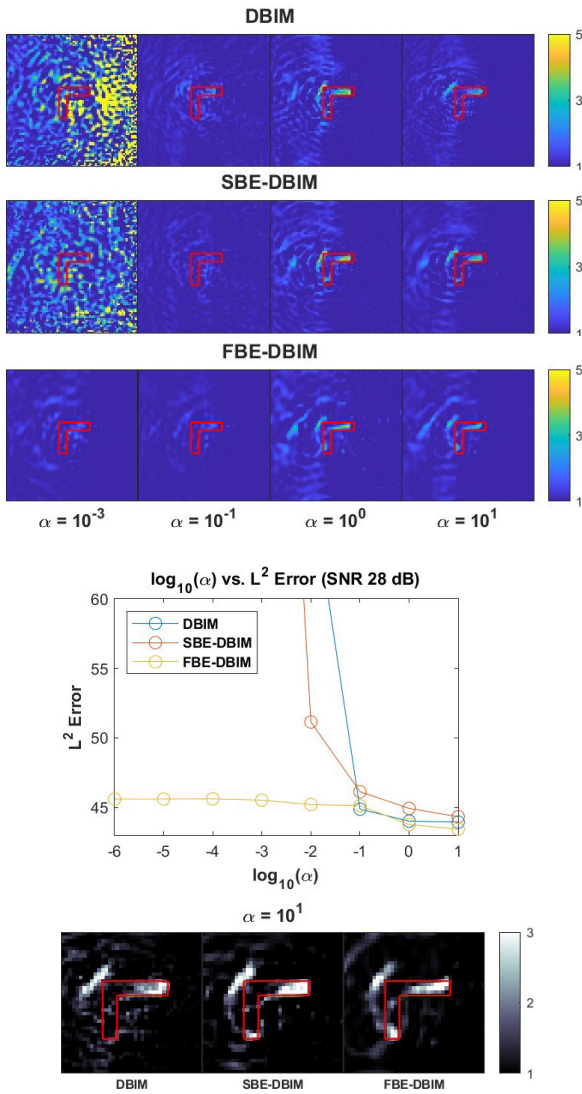


Fig. 6. Top: Reconstructed relative permittivity of high-contrast L-shaped target for four values of α with an SNR of 28 dB and an aperture size of 180°. Middle: Plot of the L^2 error in the reconstructed relative permittivity against α . Bottom: A zoomed-in plot comparing the reconstructions for $\alpha = 10^1$. The image has been rescaled to show the details.

as the Born approximation used at each iteration becomes increasingly inaccurate as the contrast of the object grows [37]. The high contrast in addition to the limited-aperture results in a more challenging inversion; however, the FBE-DBIM still provides the best results.

The relative permittivities of the lossy L-shaped target in Fig. 7 do not quite reach the true value of $\epsilon_r = 2$, which is common for lossy targets in DBIM. However, the L-shape is still very clear in each FBE-DBIM reconstruction, and the conductivity of the target is also well-represented in Fig. 8. This suggests that the proposed method is equally applicable for both lossless and lossy targets. Since the optimal choice of regularization parameter is not typically known a priori, this added robustness against the choice of α is undoubtedly an advantage of the FBE-DBIM algorithm.

Fig. 9 displays the “optimal” reconstruction of the relative permittivity for the lossless L-shaped target for an aperture size of 90° at each SNR value. This optimal reconstruction

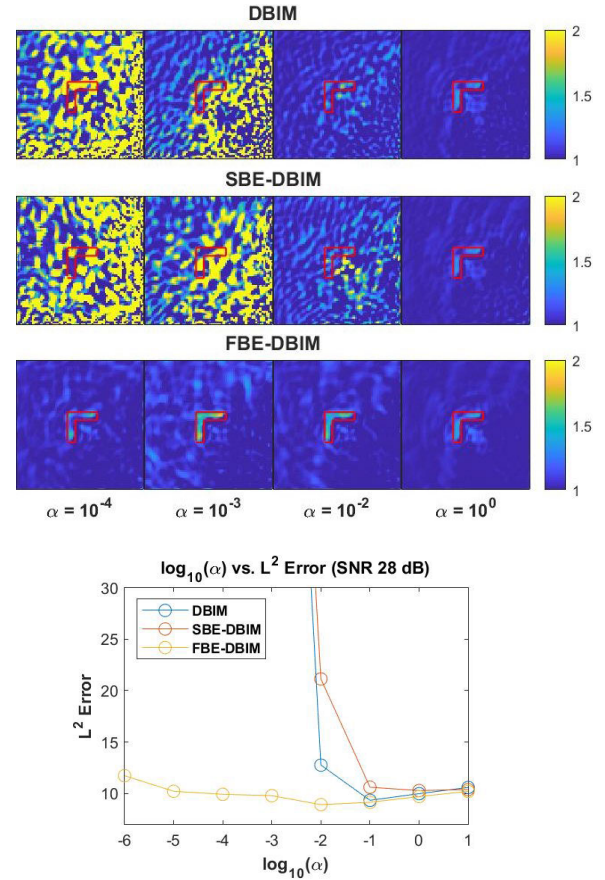


Fig. 7. Top: Reconstructed relative permittivity of lossy L-shaped target for four values of α with an SNR of 28 dB and an aperture size of 120°. Bottom: Plot of the L^2 error in the reconstructed relative permittivity against α .

was chosen by simply selecting the value of α that produced the lowest L^2 error for each of the three methods. The bottom of Fig. 9 displays the L^2 error in the permittivity reconstruction for all three methods at each SNR value. At SNR values of 42 and 28, the L-shaped figure is completely captured by the DBIM and FBE-DBIM algorithms, while the FBE-DBIM algorithm was the only one that managed to produce a reasonable reconstruction at 14 dB. None of the algorithms could manage any meaningful reconstruction at 0 dB. This plot reveals that the FBE-DBIM algorithm not only makes the inversion process more robust against the choice of α , but it was also able to produce better overall reconstructions for the lossless L-shaped target at three of the four noise levels tested.

The top of Fig. 10 shows the optimal relative permittivity reconstruction (determined again by selecting the reconstructions with the lowest L^2 error value) of the double-circle target at each aperture configuration with an SNR of 28 dB. Note that the bolder red circle in Fig. 10 denotes the circular target with a relative permittivity $\epsilon_r = 3$. The bottom of Fig. 10 displays a plot of the L^2 error for each of these reconstructions. Note that at 180° there is little difference qualitatively between the three algorithms, but as the aperture is decreased we begin to see the FBE-DBIM algorithm outperform standard DBIM and SBE-DBIM until the aperture size is reduced to 90°, in which case each algorithm performs equally poorly. This result demonstrates that the frequency beamforming enhancement

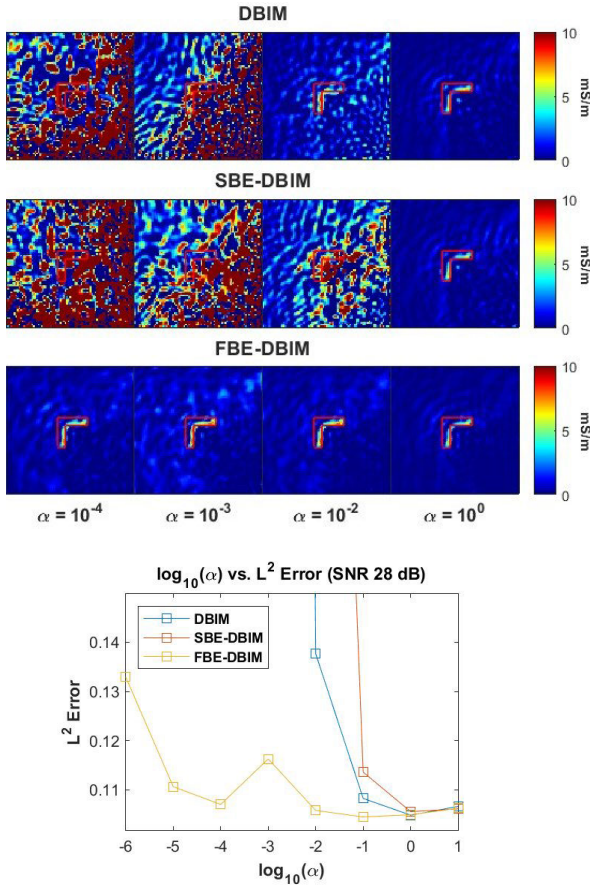


Fig. 8. Top: Reconstructed conductivity of lossy L-shaped target for four values of α with an SNR of 28 dB and an aperture size of 120° . Bottom: Plot of the L^2 error in the reconstructed conductivity against α .

improves the flexibility of the imaging algorithm to aperture size.

It is also interesting to observe the relatively poor performance of SBE-DBIM compared to the standard DBIM algorithm in Figs. 4–10. Previous work [34] saw an increase in performance for SBE-DBIM over traditional DBIM for noisy datasets in a full-aperture measurement scenario. That added robustness against noise is not seen in Fig. 9, and our results suggest that SBE-DBIM underperformed DBIM in general in a limited-aperture setting. This may be due to the increased ill-posedness of the problem introduced by the limited aperture. This observation, in addition to the inferior results of FS-DBIM seen in Fig. 4, suggests that focusing both in space and frequency is necessary in order to improve performance for limited-aperture data collection scenarios.

IV. EXPERIMENTAL RESULTS

A. Experimental Dataset

In order to test the viability of the FBE-DBIM algorithm with experimental data, we present results of inversions computed using the University of Manitoba microwave imaging dataset [38]. This dataset includes tomographic measurements of multiple metallic and dielectric targets using linearly polarized antennas, which allow for the transverse magnetic approximation to be applied. An important feature of the

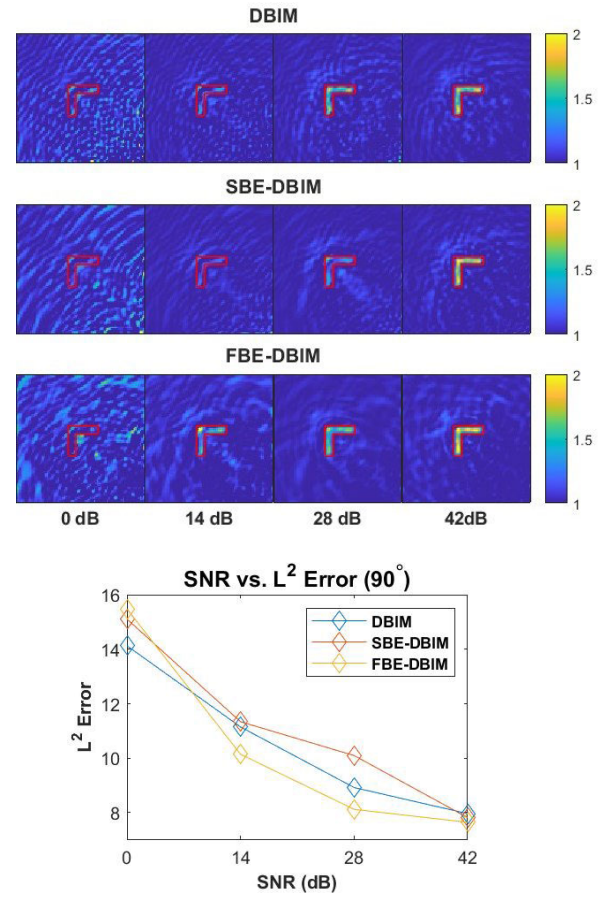


Fig. 9. Top: Reconstructed relative permittivity of lossless L-shaped target for an aperture size of 90° and four different SNR values. Bottom: Plot of the L^2 error in the reconstructed relative permittivity against SNR.

Manitoba dataset for our work is the inclusion of backscatter data, which is not present in some other well-known public repositories such as the Fresnel dataset [39], [40]. As discussed in Section I, in many applications, it is not practical to surround the target with sensors on multiple sides, necessitating the use of backscatter data, as opposed to forward scatter data. We thus select the Manitoba data to match the concept for our technique and to maintain consistency with our simulated scenarios. We leave exploration of forward-scattering imaging with frequency beamforming techniques to future work.

Data was collected using 24 double-layer Vivaldi antennas arranged in a circle, set inside of a Plexiglas imaging chamber of radius 22.2 cm. The data includes measurements from 3 to 6 GHz with 0.5 GHz frequency spacing, with monostatic data excluded from the matrix of bistatic scattering data. For our investigations, we used the data collected from two different targets: a nylon cylinder of radius 5.08 cm and length 50 cm, and a nylon cylinder of radius 1.905 cm and length 44 cm. Both cylinders have approximate relative permittivity values of 3.03 and negligible conductivity values, and each cylinder was placed in the center of the antenna array during the collection process.

B. Inversion Results

Inversions of the smaller nylon cylinder were computed using the standard DBIM, SBE-DBIM, and FBE-DBIM algorithms using datasets in which an increasing number of

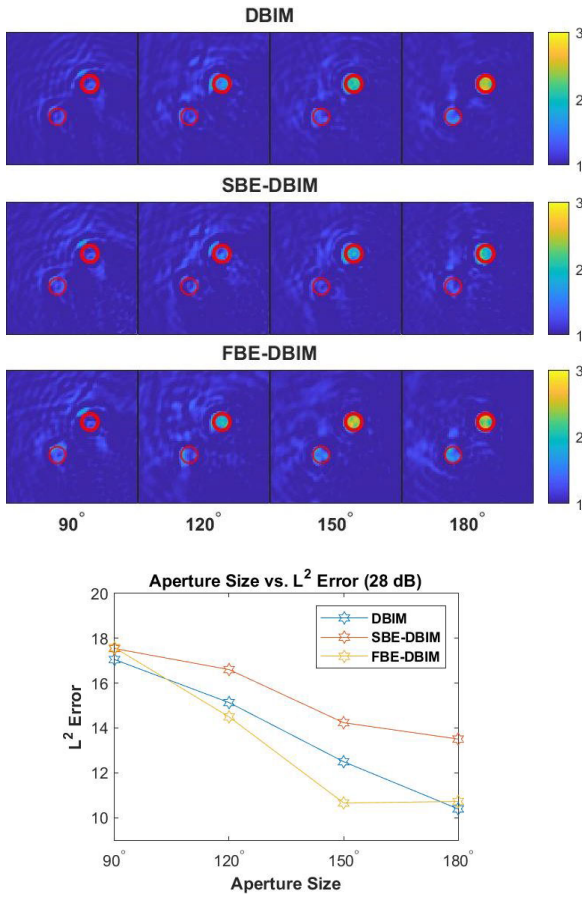


Fig. 10. Top: Reconstructed relative permittivity of double circle target at an SNR of 28 dB for four different aperture sizes. Bottom: Plot of the L^2 error in the reconstructed relative permittivity against the aperture size.

antennas were discarded, in order to approximate limited-aperture data. The spatial discretization for the inverse problem was set to 0.003 m. We do not model the antennas in the forward solution, but instead replaced them with elementary current sources in order to reduce computational complexity. To mitigate model error, we applied a calibration step similar to the one from [41] using the larger nylon cylinder of radius 5.08 cm as a calibration target. We then applied the calibration to the data from the smaller cylinder and generated an image. The calibration procedure is as follows: we first perform a forward solution of the calibration target in the imaging domain. Then, for every transmit–receive combination and every frequency, we compute the ratio $\gamma = S_{\text{cal}}/E_{\text{cal}}$, where S_{cal} is the measured signal phasor from the calibration target and E_{cal} is the simulated phasor. Lastly, we correct the measured signal phasor from the target to be imaged (given by S_{target}), by computing $E_{\text{corrected}} = S_{\text{target}}/\gamma$.

The experimental dataset presents two challenges that were not present in the numerical examples. First, there are fewer available frequencies. Second, there are fewer available antennas, and limiting the aperture used for imaging necessarily requires lowering the antenna count further. These challenges are expected to exacerbate the degree of ill-posedness of the inverse problem.

We used two frequency batches, given by $S_1 = 3 - 3.5$ GHz and $S_2 = 4 - 4.5$ GHz. We found that using frequencies above

4.5 GHz was not helpful for our limited-aperture imaging scenarios, most likely due to the higher degree of expected model mismatch for higher frequencies. It is important to note that while the 0.5-GHz frequency spacing is larger than we used for our numerical examples, this is acceptable for the experimental scenario, as the smaller imaging domain mitigates range ambiguities. In addition, while the frequencies above are larger than those used for the simulated data, the nylon cylinders are smaller than the simulated targets and thus have similar electrical lengths. For example, the electrical diameter of the simulated circle target seen in Fig. 5 at the center of the frequency band 100–450 MHz is 0.8422, while the electrical diameter of the small nylon cylinder at the center of the frequency band 3–4.5 GHz is 0.4766.

We generated reconstructions for four limited apertures of sizes 240°, 225°, 210°, and 195°. The number of antennas across the four apertures was 16, 15, 14, and 13, respectively. The aperture is oriented in the same way as the numerical example in Fig. 2, with 0° placed at the bottom of the domain and the antennas extending around the target counterclockwise. While these aperture sizes are larger than those seen in Section III-B, they are still not full-aperture and continue to allow us to test the performance of the three algorithms as the aperture size decreases. Using somewhat larger apertures was necessary for achieving faithful images due to the smaller number of available antennas. All reconstructions again used values of α evenly spaced on a logarithmic scale from 10^{-6} to 10.

Fig. 11 shows reconstructions of the relative permittivity for the nylon circle of radius 1.905 cm for four different values of α with an aperture size of 210° using 14 antennas. The four largest values of α led to the best reconstructions here, which is unsurprising given the large degree of ill-posedness present in the inverse problem. Note that in all of these reconstructions, the imaging methods successfully reconstructed the illuminated portions of the target for at least some values of α . Specifically, we are able to see the right side of the nylon circle reconstructed for DBIM at $\alpha = 10^{-1}$ and for FBE-DBIM at $\alpha = 10^{-1}$ and $\alpha = 10^0$. The results across the four values of α are encouraging, as we again see an increased resistance to changes in the regularization parameter value for the FBE-DBIM algorithm. In particular, the FBE-DBIM algorithm qualitatively appears to produce better reconstructions for all four values of α shown, as the boundary of the nylon circle is more faithfully represented and artifacts are more greatly suppressed. This is supported by the plot of the L^2 error against the regularization parameter at the bottom of Fig. 11, in which FBE-DBIM matches or outperforms the other two algorithms for every value of α . For this plot, the ground-truth target used to calculate the L^2 error was assigned a radius of 1.905 cm and a relative permittivity of 3.03, as given in [38]. Note that we have excluded the L^2 error values for $\log_{10}(\alpha) = -6$ and $\log_{10}(\alpha) = -5$ in this plot for readability purposes, but FBE-DBIM also outperforms the other two algorithms at these values.

Fig. 12 displays the “best” reconstruction for each of the three methods at each of the four different aperture sizes. These optimal reconstructions were selected by analyzing the

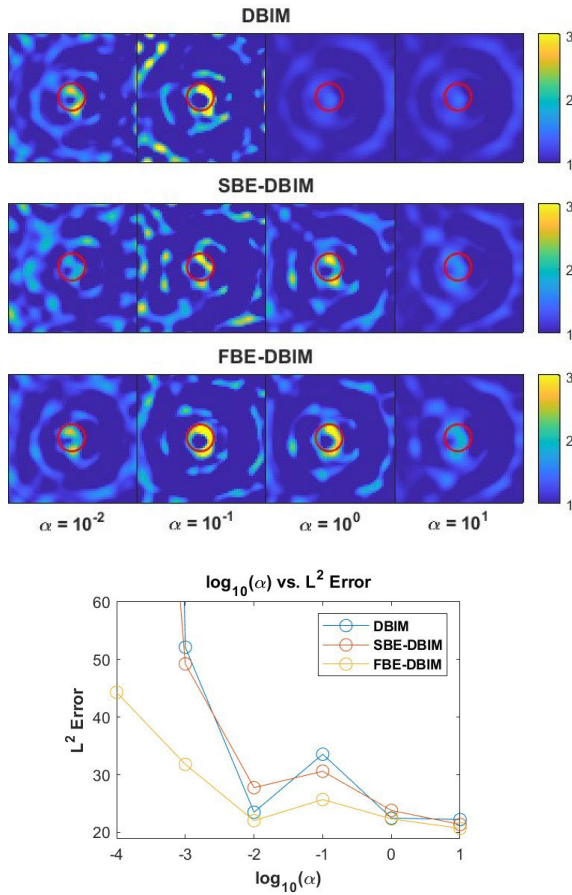


Fig. 11. Top: Reconstructed relative permittivity of circular nylon target with a radius of 1.905 cm for four values of α using experimental data collected with an aperture size of 210° and 14 antennas. Bottom: Plot of the L^2 error in the reconstructed relative permittivity against α .

reconstructions for all eight values of α and selecting the reconstructions that simultaneously best matched the boundary of the nylon circle while mitigating artifacts due to noise. The results are again convincing, as we see the FBE-DBIM algorithm consistently able to reconstruct the boundary of the circle with more accuracy as compared to the other two methods while also doing an admirable job of suppressing artifacts. Note also that at 240° the DBIM and FBE-DBIM methods are able to reconstruct roughly three-quarters of the boundary, but both DBIM and SBE-DBIM begin to degrade and display more artifacts as the aperture decreases. However, the FBE-DBIM algorithm preserves at least half of the boundary of the circle with high fidelity at every aperture size and does not display increased artifacts as the aperture decreases.

The middle of Fig. 12 displays the L^2 error against the aperture size at pixels located inside the support of the scatterer, while the bottom of Fig. 12 shows the same plot but for pixels located outside the support of the scatterer. This slight change in the presentation of the L^2 error is due to the difference in experimental imagery compared with simulated imagery, including a greater number of background artifacts, which is reasonable for reconstructions from experimental data. These plots match well the visual conclusions made above, as the FBE-DBIM algorithm outperforms both other algorithms for every aperture size at pixels inside of the scatterer. While SBE-DBIM does a better job at pixels outside

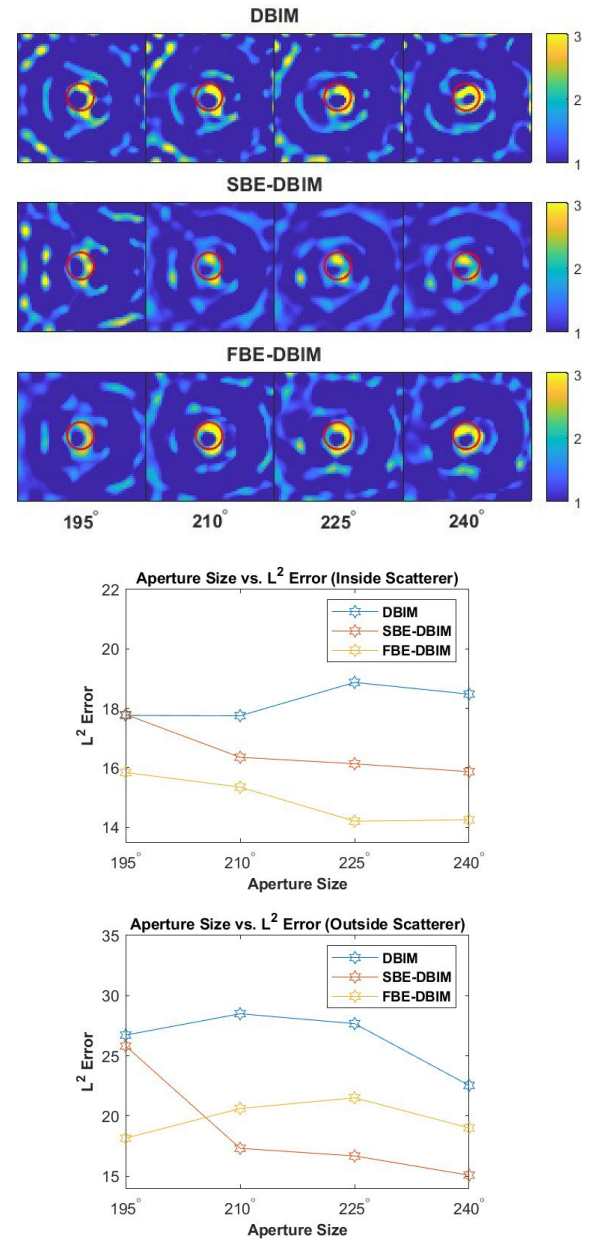


Fig. 12. Top: Reconstructed relative permittivity of circular nylon target with a radius of 1.905 cm using experimental data collected from four different aperture sizes. Middle: Plot of the L^2 error in the reconstructed relative permittivity against the aperture size at pixels located inside of the scatterer. Bottom: Plot of the L^2 error in the reconstructed relative permittivity against the aperture size at pixels located outside of the scatterer.

of the scatterer for aperture sizes of 210° , 225° , and 240° , it struggles to visually match the boundary of the circle. At the lowest aperture value of 195° , FBE-DBIM produces a better reconstruction both inside and outside the scatterer. This suggests that the FBE-DBIM algorithm indeed increases the robustness of the DBIM algorithm against limited-aperture information.

V. CONCLUSION

We have presented a frequency beamforming enhancement to the previously proposed SBE-DBIM algorithm for use in a limited-aperture imaging scenario. Numerical results showed that the FBE-DBIM algorithm outperformed both DBIM and

SBE-DBIM for various targets in several apertures and SNR configurations and dramatically improved the robustness of the algorithm against the choice of regularization parameter. Experimental results reinforced this conclusion and showed that even with challenges presented by open-source datasets, FBE-DBIM is able to improve the fidelity of reconstructions as the size of the aperture decreases compared with DBIM and SBE-DBIM.

There are many different directions and applications that future work could consider. This article examines a number of targets in general measurement scenarios, but it would be interesting to expand our exploration to include specific applications including medical imaging, GPR, and through-wall imaging. The frequency beamforming enhancement can also be applied to other quantitative methods, such as contrast source inversion. In addition, the technique could be even more beneficial when extended to hybrid quantitative–qualitative inverse scattering approaches [42], which could leverage the benefits of both strategies to further mitigate the ill-posedness of the problem.

REFERENCES

- [1] R. Marklein, J. Miao, M.-U. Rahman, and K. J. Langenberg, "Inverse scattering and imaging in NDT: Recent applications and advances," in *Proc. Eur. Conf. Non-Destructive Test.*, Jan. 2006, pp. 1–8.
- [2] A. P. Annan, "Electromagnetic principles of ground penetrating radar," in *Ground Penetrating Radar: Theory and Applications*, vol. 1. Amsterdam, The Netherlands: Elsevier, 2009, pp. 1–37.
- [3] S. Semenov, "Microwave tomography: Review of the progress towards clinical applications," *Phil. Trans. Roy. Soc. A, Math., Phys. Eng. Sci.*, vol. 367, no. 1900, pp. 3021–3042, Aug. 2009.
- [4] A. J. Devaney, "Inverse scattering as a form of computed tomography," *Proc. SPIE*, vol. 358, pp. 10–16, Feb. 1982.
- [5] J. Cai and G. A. McMechan, "2-D ray-based tomography for velocity, layer shape, and attenuation from GPR data," *Geophysics*, vol. 64, no. 5, pp. 1579–1593, Sep. 1999.
- [6] J. R. Ernst, H. Maurer, A. G. Green, and K. Holliger, "Full-waveform inversion of crosshole radar data based on 2-D finite-difference time-domain solutions of Maxwell's equations," *IEEE Trans. Geosci. Remote Sens.*, vol. 45, no. 9, pp. 2807–2828, Sep. 2007.
- [7] J. R. Ernst, A. G. Green, H. Maurer, and K. Holliger, "Application of a new 2D time-domain full-waveform inversion scheme to crosshole radar data," *Geophysics*, vol. 72, no. 5, pp. J53–J64, Sep. 2007.
- [8] S. Kuroda, M. Takeuchi, and H. J. Kim, "Full-waveform inversion algorithm for interpreting crosshole radar data: A theoretical approach," *Geosci. J.*, vol. 11, no. 3, pp. 211–217, Sep. 2007.
- [9] R. E. Kleinman and P. M. V. D. Berg, "A modified gradient method for two-dimensional problems in tomography," *J. Comput. Appl. Math.*, vol. 42, no. 1, pp. 17–35, Sep. 1992.
- [10] P. M. Van Den Berg and R. E. Kleinman, "A contrast source inversion method," *Inverse Prob.*, vol. 13, no. 6, p. 1607, Dec. 1997.
- [11] Y. M. Wang and W. C. Chew, "An iterative solution of the two-dimensional electromagnetic inverse scattering problem," *Int. J. Imag. Syst. Technol.*, vol. 1, no. 1, pp. 100–108, 1989.
- [12] W. C. Chew and Y. M. Wang, "Reconstruction of two-dimensional permittivity distribution using the distorted born iterative method," *IEEE Trans. Med. Imag.*, vol. 9, no. 2, pp. 218–225, Jun. 1990.
- [13] X. Liu and J. Sun, "Data recovery in inverse scattering: From limited-aperture to full-aperture," *J. Comput. Phys.*, vol. 386, pp. 350–364, Jun. 2019.
- [14] K. Ito, B. Jin, and J. Zou, "A direct sampling method to an inverse medium scattering problem," *Inverse Problems*, vol. 28, no. 2, Feb. 2012, Art. no. 025003.
- [15] K. Ito, B. Jin, and J. Zou, "A direct sampling method for inverse electromagnetic medium scattering," *Inverse Problems*, vol. 29, no. 9, Sep. 2013, Art. no. 095018.
- [16] S. Kang, M. Lambert, C. Y. Ahn, T. Ha, and W.-K. Park, "Single- and multi-frequency direct sampling methods in a limited-aperture inverse scattering problem," *IEEE Access*, vol. 8, pp. 121637–121649, 2020.
- [17] C. Y. Ahn, T. Ha, and W.-K. Park, "Direct sampling method for identifying magnetic inhomogeneities in limited-aperture inverse scattering problem," *Comput. Math. Appl.*, vol. 80, no. 12, pp. 2811–2829, Dec. 2020.
- [18] W.-K. Park, "A novel study on the MUSIC-type imaging of small electromagnetic inhomogeneities in the limited-aperture inverse scattering problem," *J. Comput. Phys.*, vol. 460, Jul. 2022, Art. no. 111191.
- [19] R. Schmidt, "Multiple emitter location and signal parameter estimation," *IEEE Trans. Antennas Propag.*, vol. AP-34, no. 3, pp. 276–280, Mar. 1986.
- [20] J. W. Odendaal, E. Barnard, and C. W. I. Pistorius, "Two-dimensional superresolution radar imaging using the MUSIC algorithm," *IEEE Trans. Antennas Propag.*, vol. 42, no. 10, pp. 1386–1391, Oct. 1994.
- [21] M. Benedetti, M. Donelli, D. Lesselier, and A. Massa, "A two-step inverse scattering procedure for the qualitative imaging of homogeneous cracks in known host media—preliminary results," *IEEE Antennas Wireless Propag. Lett.*, vol. 6, pp. 592–595, 2007.
- [22] M. J. Burfeindt and H. F. Alqadah, "Phase-encoded linear sampling method imaging of conducting surfaces from full and limited synthetic apertures," *IEEE Open J. Antennas Propag.*, vol. 3, pp. 1191–1205, 2022.
- [23] D. Colton, H. Haddar, and M. Piana, "The linear sampling method in inverse electromagnetic scattering theory," *Inverse Problems*, vol. 19, no. 6, pp. S105–S137, Dec. 2003.
- [24] L. Audibert and H. Haddar, "The generalized linear sampling method for limited aperture measurements," *SIAM J. Imag. Sci.*, vol. 10, no. 2, pp. 845–870, Jan. 2017.
- [25] L. Audibert and H. Haddar, "A generalized formulation of the linear sampling method with exact characterization of targets in terms of farfield measurements," *Inverse Problems*, vol. 30, no. 3, Mar. 2014, Art. no. 035011.
- [26] I. Catapano, L. Crocco, Y. Krellmann, G. Trilitzsch, and F. Soldovieri, "A tomographic approach for helicopter-borne ground penetrating radar imaging," *IEEE Geosci. Remote Sens. Lett.*, vol. 9, no. 3, pp. 378–382, May 2012.
- [27] M. Ambrosanio, M. T. Bevacqua, T. Isernia, and V. Pascazio, "The tomographic approach to ground-penetrating radar for underground exploration and monitoring: A more user-friendly and unconventional method for subsurface investigation," *IEEE Signal Process. Mag.*, vol. 36, no. 4, pp. 62–73, Jul. 2019.
- [28] M. Ambrosanio, M. T. Bevacqua, T. Isernia, and V. Pascazio, "Performance analysis of tomographic methods against experimental contactless multistatic ground penetrating radar," *IEEE J. Sel. Topics Appl. Earth Observ. Remote Sens.*, vol. 14, pp. 1171–1183, 2021.
- [29] L. Lo Monte, D. Erricolo, F. Soldovieri, and M. C. Wicks, "Radio frequency tomography for tunnel detection," *IEEE Trans. Geosci. Remote Sens.*, vol. 48, no. 3, pp. 1128–1137, Mar. 2010.
- [30] M. Zhong, Y. Chen, J. Li, and F. Han, "Reconstruction of subsurface objects by LSM and FWI from limited-aperture electromagnetic data," *IEEE Trans. Geosci. Remote Sens.*, vol. 60, 2022, Art. no. 2003011.
- [31] S. Takahashi, K. Suzuki, T. Hanabusa, and S. Kidera, "Microwave subsurface imaging method by incorporating radar and tomographic approaches," *IEEE Trans. Antennas Propag.*, vol. 70, no. 11, pp. 11009–11023, Nov. 2022.
- [32] M. Slaney, A. C. Kak, and L. E. Larsen, "Limitations of imaging with first-order diffraction tomography," *IEEE Trans. Microw. Theory Techn.*, vol. MTT-32, no. 8, pp. 860–874, Aug. 1984.
- [33] M. T. Bevacqua, S. Di Meo, L. Crocco, T. Isernia, and M. Pasian, "Millimeter-waves breast cancer imaging via inverse scattering techniques," *IEEE J. Electromagn., RF Microw. Med. Biol.*, vol. 5, no. 3, pp. 246–253, Sep. 2021.
- [34] M. J. Burfeindt, J. D. Shea, B. D. Van Veen, and S. C. Hagness, "Beamforming-enhanced inverse scattering for microwave breast imaging," *IEEE Trans. Antennas Propag.*, vol. 62, no. 10, pp. 5126–5132, Oct. 2014.
- [35] S. Ziegler and M. J. Burfeindt, "Frequency beamforming-enhanced DBIM for limited-aperture quantitative imaging," in *Proc. USNC-URSI NRSM*, Jan. 2022, pp. 173–174.
- [36] D. W. Winters, J. D. Shea, P. Kosmas, B. D. Van Veen, and S. C. Hagness, "Three-dimensional microwave breast imaging: Dispersive dielectric properties estimation using patient-specific basis functions," *IEEE Trans. Med. Imag.*, vol. 28, no. 7, pp. 969–981, Jul. 2009.
- [37] O. S. Haddadin, "Ultrasound inverse scattering for tomographic imaging and self-focusing arrays," Ph.D. dissertation, Dept. Elect. Eng., Syst., Univ. Michigan, Ann Arbor, MI, USA, 1997.

- [38] C. Gilmore, A. Zakaria, P. Mojabi, M. Ostadrahimi, S. Pistorius, and J. L. Vetri, "The University of Manitoba microwave imaging repository: A two-dimensional microwave scattering database for testing inversion and calibration algorithms [measurements corner]," *IEEE Antennas Propag. Mag.*, vol. 53, no. 5, pp. 126–133, Oct. 2011.
- [39] K. Belkebir and M. Saillard, "Testing inversion algorithms against experimental data," *Inverse Problems*, vol. 17, no. 6, pp. 1565–1571, 2001.
- [40] K. Belkebir and M. Saillard, "Testing inversion algorithms against experimental data: Inhomogeneous targets," *Inverse Problems*, vol. 21, no. 6, pp. S1–S3, Dec. 2004.
- [41] M. J. Burfeindt and H. F. Alqadah, "Boundary-Condition-Enhanced linear sampling method imaging of conducting targets from sparse receivers," *IEEE Trans. Antennas Propag.*, vol. 70, no. 3, pp. 2246–2260, Mar. 2022.
- [42] R. Palmeri, M. T. Bevacqua, L. Crocco, T. Isernia, and L. Di Donato, "Microwave imaging via distorted iterated virtual experiments," *IEEE Trans. Antennas Propag.*, vol. 65, no. 2, pp. 829–838, Feb. 2017.



Scott J. Ziegler received the B.S. degree in mathematics and the B.A. degree in physics from the University of Kansas, Lawrence, KS, USA, in 2016, and the M.S. and Ph.D. degrees in mathematics from Colorado State University, Fort Collins, CO, USA, in 2018 and 2022, respectively.

He has been with United States Naval Research Laboratory, Washington, DC, USA, since 2021. His research interests include inverse problems, radar imaging, and stochastic processes.



Matthew J. Burfeindt (Senior Member, IEEE) received the B.S. degree in electrical engineering from the University of Nebraska-Lincoln, Lincoln, NE, USA, in 2008, and the M.S. and Ph.D. degrees in electrical engineering from the University of Wisconsin-Madison, Madison, WI, USA, in 2011 and 2013, respectively.

He was with the Air Force Research Laboratory, Eglin AFB, FL, USA, between 2013 and 2018. Since 2018, he has been with United States Naval Research Laboratory, Washington, DC, USA. He is currently an Adjunct Professor with the Department of Electrical Engineering, Wright State University, Dayton, OH, USA. His research interests include inverse scattering, radar imaging, and radar signal processing.

Dr. Burfeindt was a recipient of the Department of Defense SMART Scholarship for Service from 2008 to 2013. He also received the First Prize Award in the Ernest K. Smith USNC-URSI Student Paper Competition at the 2012 National Radio Science Meeting, the Air Force Research Laboratory Munitions Directorate Scientific/Technical Achievement of the Year Award (Category II) in 2017, and the Naval Research Laboratory Alan Berman Research Publication Award in 2022. He is the Chair of Washington/Northern Virginia chapter of the IEEE Antennas and Propagation Society. He is also an Associate Editor of *IET Electronics Letters*.